

Exploring Multiferroic Behavior in CaZnFeOsO_6 : A Novel Layered $3d$ - $5d$ Double Perovskite Compound

Deepti Rajpoot¹, Paresh C. Rout², Nikita Acharya³, and Varadharajan Srinivasan^{1*}

¹Department of Chemistry, Indian Institute of Science Education and Research Bhopal, Bhopal 462 066, India

²Consiglio Nazionale delle Ricerche (CNR-SPIN),

Unità di Ricerca presso Terzi c/o Università "G. D'Annunzio," 66100 Chieti, Italy and

³Department of Physics, Indian Institute of Information Technology Bhopal, Bhopal 462066, India

(Dated: August 22, 2024)

We present a novel multiferroic double perovskite compound, CaZnFeOsO_6 (CZFOO), exhibiting combined ferroelectric and ferrimagnetic properties. Through *ab initio* density functional theory calculations, we predict CZFOO as a unique example of an A-site and B-site ordered double perovskite structure, $\text{AA}'\text{BB}'\text{O}_6$. In this compound, Fe^{3+} and Os^{5+} ions generate substantial magnetization, while Ca^{2+} and Zn^{2+} ions create a layerwise polar environment, resulting in a synergistic combination for multiferroicity. We determine the magnitude of the spontaneous polarization, $|\text{Ps}|$, to be $16.8 \mu\text{C}/\text{cm}^2$, and the magnetic moment is approximately $2\mu_B$ per formula unit. The remarkable ferroelectric and ferrimagnetic behaviors exhibited by CZFOO make it a promising candidate for various device applications. Despite the significant magnetization and polarization observed, surpassing those of other double perovskites, we find a weak spin-orbit coupling, leading to the absence of any significant magnetoelectric effect in CZFOO. Our findings shed light on the potential of CZFOO as a multiferroic material and provide insights into the intricate interplay between ferroelectricity and ferrimagnetism in double perovskite compounds.

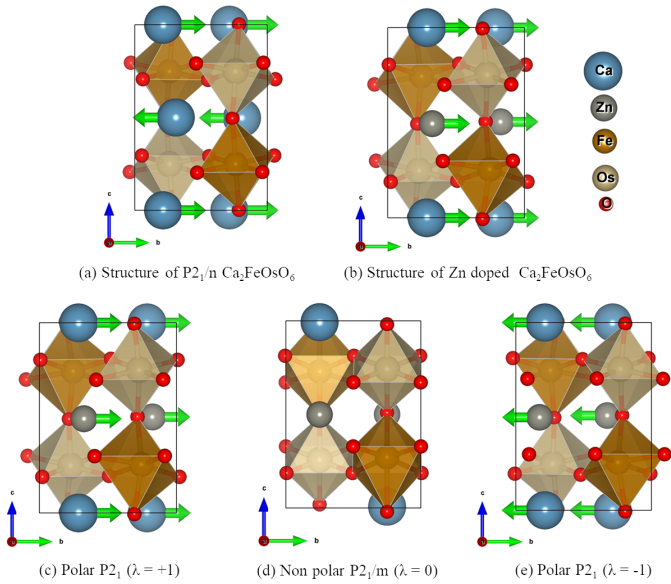


FIG. 1. Structures of $\text{Ca}_2\text{FeOsO}_6$ and CaZnFeOsO_6 . Blue, gray, dark brown, light brown and red colors spheres represent Ca, Zn, Fe, Os, and O atoms respectively. The green arrow represents the displacement of Ca and Zn atoms.

INTRODUCTION:

Transition metal oxide perovskites are known for their wide range of applications in electronics and data storage devices due to their exciting properties such as magnetism, ferroelectricity, superconductivity, colossal magnetoresistance, ionic conductivity, dielectric properties, multiferroicity, and magnetoelectric effect [1]. In partic-

ular, transition metal perovskites (ABO_3) with $3d$ cations at the B-site have been extensively explored. Similarly, double perovskite (DP) oxides ($\text{A}_2\text{BB}'\text{O}_6$), where B and B' represent two different transition metal cations, A represents alkaline earth/rare earth metal cations, and O represents oxygen, are particularly interesting from a magnetic properties perspective. Recently, $3d$ - $5d$ transition metal double perovskite oxides, where one of the B-site cations belongs to the $3d$ series and the second to the $5d$ series, have been investigated due to their fascinating properties such as half-metallic ferromagnetism (HM-FM), large tunneling magnetoresistance (TMR), and high Curie temperature (T_c) [2–4]. These DP oxides, benefiting from the higher spin-orbit coupling in $5d$ ions along with their stronger hybridization with oxygen, hold potential for applications in nonvolatile memory storage, spintronics, and other areas.

The interdependence of spin, orbital, lattice, and charge degrees of freedom in these materials can lead to multiferroic behavior and frequently lead to the coupling of multiple ferroic orders. This coupling refers to the interconnected nature and mutual influence between different types of ferroic phenomena, such as ferroelectricity, ferromagnetism, and ferroelasticity. This intricate interplay results in the emergence of complex physical properties and holds significant potential for various technological applications [5, 6].

There are several multiferroic double perovskite materials, such as $\text{Bi}_2\text{NiMnO}_6$ [7], $\text{Bi}_2\text{FeCrO}_6$ [8], and $\text{Bi}_2\text{MnReO}_6$ [9], which exhibit electric polarization and magnetization near room temperature. In a recent study, it was demonstrated that by mixing cations at the A-site ($\text{R}_2\text{NiMnO}_6/\text{La}_2\text{NiMnO}_6$, where R is a rare-earth ion), the multiferroic properties can be tuned near-room tem-

perature. However, the magnetic critical temperature remains below room temperature for the best ferroelectric candidate in the series [10, 11].

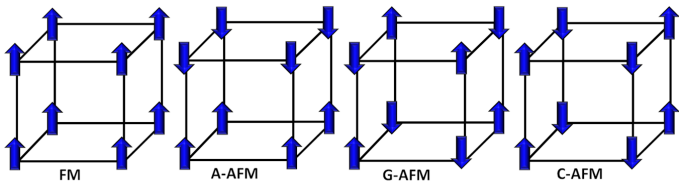


FIG. 2. Magnetic ordering

Recently, the double perovskite $\text{Ca}_2\text{FeOsO}_6$ (CFO) was synthesized [12]. CFO exhibits a non-polar structure with space group $P2_1/n$, and it displays strong ferrimagnetic behavior at high temperatures, around 320K. Additionally, the CFO shows near half-metallic behavior. The non-polar structure of CFO is stabilized by a layer-wise anti-polar displacement of Ca^{2+} ions (see Fig. 1) [13]. On the other hand, $\text{Zn}_2\text{FeOsO}_6$ (ZFO) has been predicted to have a polar structure, with a space group of $R3$. It exhibits a large polarization of $54.7 \mu\text{C}/\text{cm}^2$ and magnetization of $2\mu_B$ per unit cell above room temperature ($T_c \approx 394\text{K}$), along with an insulating behavior [14]. The LN-type structural distortion in ZFO is responsible for its ferroelectric polarization [15, 16]. However, the magnetic easy axis lies in the plane, making it unsuitable for high-density data storage applications [17–19]. It is important to note that the bulk structure or the thin-film form of ZFO is yet to be realized experimentally. In another recent study, it has been reported that the superlattice $\text{Ca}_2\text{FeOsO}_6/\text{Sr}_2\text{FeOsO}_6$ exhibits room temperature multiferroicity with hybrid improper ferroelectric polarization up to $20 \mu\text{C}/\text{cm}^2$, despite the different Glazer tilting patterns of its components [20]. However, there is no report of magnetic anisotropic behavior in this study, despite the presence of heavy B-site cations. Furthermore, it has been shown that the electronic properties of these double perovskites can be dramatically altered by varying the size of the A-site cations [13, 21].

Motivated by these studies, we investigated the potential for inducing multiferroicity in CFO by replacing half of the Ca^{2+} ions with Zn^{2+} . Note that the recent layer-wise growth technique makes it possible to deposit smooth films layer by layer with high quality [22]. Our predictions led to the discovery of a layered compound named CaZnFeOsO_6 (CZFOO), where the A-site cations alternate in layers, as illustrated in Figure 1(b). Surprisingly, our findings reveal a regular polar structure ($P2_1$) with all A-site cations displaced in one direction, which is contrary to previous similar studies. We have successfully demonstrated the robust multiferroic behavior of the superlattice, with a ferroelectric polarization of $16.75 \mu\text{C}/\text{cm}^2$ and magnetic moments of $2\mu_B$ per formula unit. Moreover, by incorporating the spin-orbit

coupling (SOC), we have revealed the exciting possibility of a weak coupling between the ferrimagnetic and ferroelectric properties, resulting in the induction of a magnetoelectric effect in the system. These findings highlight the potential for exploiting the interplay between magnetism and ferroelectricity, opening up new avenues for multifunctional device applications.

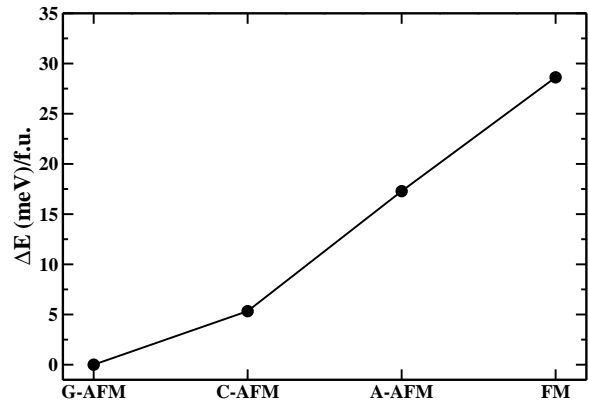


FIG. 3. Energy difference from most stable magnetic structure (G-AFM) to other magnetic structure

COMPUTATIONAL DETAILS:

Calculations were performed using the first-principles Density Functional Theory (DFT) method. Specifically, we utilized a spin-polarized Generalized Gradient Approximation (GGA) with Hubbard correction approach based on the Perdew-Burke-Ernzerhof (PBE) exchange-correlation functional [23, 24]. The Quantum ESPRESSO code [25] was employed, using a plane wave basis approach. To account for correlation effects, Hubbard U values of 5.0 eV for Fe atoms and 2.0 eV for Os atoms were employed. Brillouin zone integration was performed using an $8 \times 8 \times 8$ Monkhorst-Pack k-point mesh, and a plane-wave basis with a kinetic-energy cutoff of 90 Ry and a charge density cutoff of 900 Ry was used. For density of state (DOS) calculations, the Monkhorst-Pack k-point mesh was increased to $16 \times 16 \times 16$.

Structural optimization was conducted using a 20-atom monoclinic supercell, starting from experimental lattice parameters of $\text{Ca}_2\text{FeOsO}_6$. The optimization process continued until the atomic forces were less than 0.25 meV/Å, per atom, and the energy was minimized to a target value of 13.6×10^{-11} eV. Volumes and lattice parameters were optimized to ensure stresses were below 0.1 kbar. Polarization calculations were performed using the Berry phase method [26]. Spin-orbit coupling (SOC) was

included in the calculations using the GGA+ U functional within the Vienna Ab initio Simulation Package (VASP) [27–29]. Plane-wave cutoff energy of 900 eV and a $9\times 9\times 9$ k-point mesh were used for Brillouin zone sampling in the 20-atom unit cell. For dynamical stability calculations, Density Functional Perturbation Theory (DFPT) was employed with a 20-atom cell and the finite difference method. Supercells with 80 and 160 atoms ($2\times 2\times 1$ and $2\times 2\times 2$, respectively) were used in the finite difference approach [30–32]. Phonon calculations were performed with a $4\times 4\times 4$ k-point grid, and a phonon convergence criterion of 10^{-24} was employed, considering that the energy difference between the $8\times 8\times 8$ and $4\times 4\times 4$ k-point grids was less than 5 meV.

RESULTS AND DISCUSSION:

Starting with the experimental structure of monoclinic ($P2_1/n$) $\text{Ca}_2\text{FeOsO}_6$, we replaced half of the A-site Ca atoms with Zn atoms to form a 1:1 CaZnFeOsO_6 superlattice. Next, we fully optimized the ionic positions and cell parameters using the GGA+ U method. The optimized cell parameters are as follows: $a=5.32048$ Å, $b=5.60021$ Å, $c=7.75288$ Å, and $\beta = 90.084^\circ$, indicating a monoclinic space group ($P2_1$). Although we considered the possibility of the $R3$ space group in our study, the polar $P2_1$ structure was found to be lower in energy (192 meV/formula unit). Notably, we observed a unique feature in this superlattice: a polar displacement of all the A-site cations along the y-axis while maintaining the $P2_1$ symmetry. This distinguishes it from other superlattices where the ferroelectric polarization arises from antipolar displacements along the y-axis with varying magnitudes [13, 20, 21]. The presence of this unique feature suggests the potential for a large ferroelectric polarization at room temperature.

Next, we predicted the magnetic ground state by considering various possible fundamental collinear magnetic orderings, namely ferromagnetic (FM), antiferromagnetic with A-type ordering (A-AFM), antiferromagnetic with C-type ordering (C-AFM), and antiferromagnetic with G-type ordering (G-AFM), as depicted in Figure 2. Interestingly, we discovered that the superlattice prefers G-AFM ordering, similar to its components, resulting in a magnetic moment of $2 \mu_B$ /formula unit. Figure 3 presents the obtained total energies relative to the global minimum, clearly indicating that the $P2_1$ symmetry with G-AFM ordering is the most favorable among other magnetic orderings. To ensure the stability of this superlattice, we calculated the phonon dispersion using the frozen phonon approach [31, 32]. Figure 4 displays the calculated phonon dispersion. Remarkably, the absence of imaginary frequencies confirms that the superlattice is dynamically stable.

To confirm ferroelectricity in the compound, we cal-

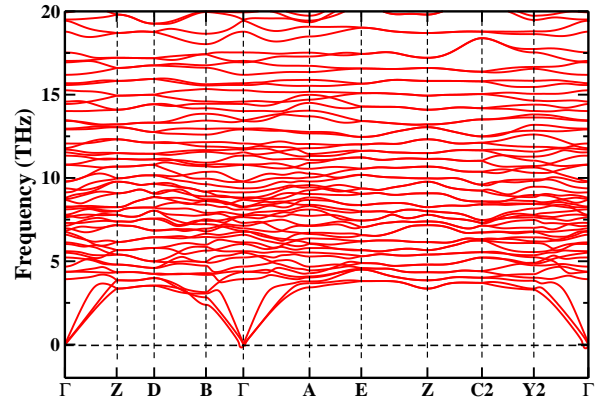


FIG. 4. Phonon dispersion for the polar CZFOO using finite difference for $2\times 2\times 2$ supercell.

culated the polarization using the Berry phase approach. Interestingly, our calculations revealed a sizable polarization of $16.8 \mu\text{C}/\text{cm}^2$ which surpasses the previously demonstrated values of $9.0 \mu\text{C}/\text{cm}^2$ in the $\text{R}_2\text{NiMnO}_6/\text{La}_2\text{NiMnO}_6$ series (where R is a rare-earth ion) [10], as well as the reported room temperature ferroelectric polarization of $8.0 \mu\text{C}/\text{cm}^2$ in the unstrained $\text{Ca}_2\text{FeOsO}_6/\text{Sr}_2\text{FeOsO}_6$ superlattice [20]. The polar displacement of all A-site cations is a result of the increasing out-of-plane tilting angles due to the doping of the smaller Zn cations at the A-sites. This increase in tilting angle occurs as the oxygen anions shift towards the smaller Zn cations, forming stronger covalent-type bonds.

To further demonstrate the ferroelectric nature of the system, we calculated the energy barrier using a paraelectric structure ($P2_1/n$). The paraelectric phase was obtained using PSEUDOSYMMETRY and AMPLIMODES [33]. We find that the activation barrier without a structurally optimized paraelectric phase is 2.23 eV per cell. However, the barrier significantly reduces to 0.62 eV with an optimized paraelectric phase (see Figure 5). This indicates that the polarization can be easily switched.

Electronic and magnetic properties:

In this section, we have analyzed the electronic structure of CZFOO. Figure 7 displays the projected density of states for both the polar and non-polar (paraelectric) structures. It is observed that both structures are narrow bandgap semiconductors. In the polar structure, the valence band maximum is primarily contributed by the strong hybridization between Os ($5d$) and O ($2p$) orbitals. On the other hand, the conduction band minimum is

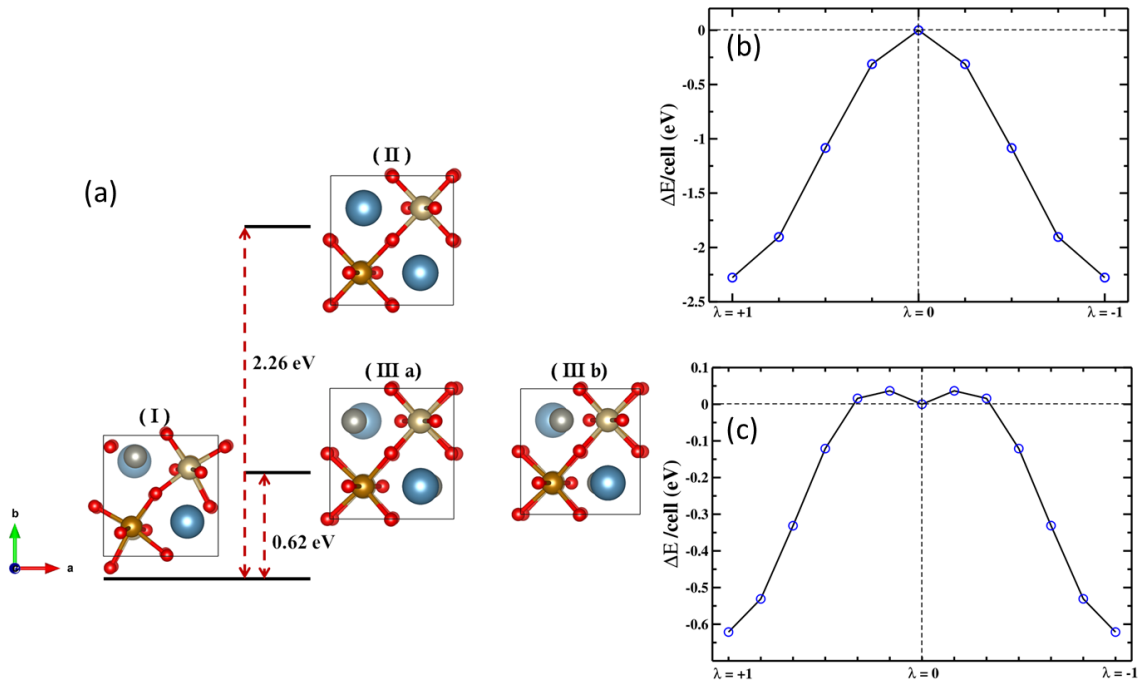


FIG. 5. Comparison of energy barriers between polar and non-polar structures. In Figure (a), (I) represents a polar structure (space group $P2_1$), while (II) depicts an unoptimized non-polar structure (space group $P2_1/m$). Intermediate structures (IIIa) and (IIIb) are shown after relaxing atomic positions (both with space group $P2_1/m$). Figure (b) illustrates the energy barrier path utilizing the unoptimized non-polar structure (II), while (c) demonstrates the energy barrier path using the optimized non-polar structure post atomic position relaxation (IIIa)/(IIIb).

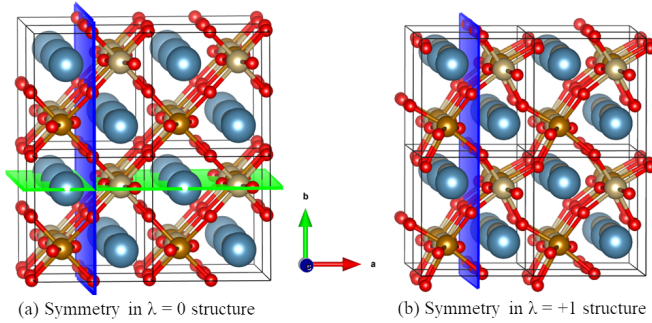


FIG. 6. Symmetry in $\lambda = 0$ and $\lambda = +1$ structure. Here blue plane is used to indicate the 2_1 screw axis and a green plane is used to indicate the mirror plane.

dominated by the hybridization between Os ($5d$) and O $2(p)$ orbitals in the minority spin channel. In contrast, the hybridized Fe ($3d$) and O $2(p)$ orbitals play a dominant role in the majority spin channel. Our investigation indicates that the lowest energy magnetic structure corresponds to a ferrimagnetic ordering, with antialigned $3d$ and $5d$ ions. The electronic configuration analysis reveals that Os adopts a high-spin $5+$ oxidation state with half-filled t_{2g} and empty eg orbitals (t_{2g}^3, e_g^0), whereas Fe adopts a high-spin $3+$ oxidation state with a d^5 configuration (t_{2g}^3, e_g^2). This conclusion is further supported

by analyzing the occupation numbers of the d orbitals, obtained by summing the projections of the Kohn-Sham states onto the d orbitals.

Due to the specific electronic shell configurations and the nearly 140° (150°) in-plane (out-of-plane) Fe-O-Os bond angles, the magnetic moments of the Fe and Os sublattices couple via antiferromagnetic superexchange mechanisms. Consequently, a ferrimagnetic ordering is observed in CZFOO, with each formula unit exhibiting a magnetic moment of $2\mu_B$. Given that both constituent compounds (CFO and ZFO) exhibit magnetism above room temperature, it is anticipated that this superlattice will display magnetism above room temperature as well. The electronic band structure analysis reveals that the polar structure of CZFOO is an indirect band gap semiconductor (see Fig.8).

Structural analysis and origin of polarization:

To further characterize the origin of ferroelectric polarization, we have studied the structural distortion and performed symmetry mode analysis. Despite the polar displacement of A-site cations, we observe an $a^-a^+c^+$ tilting pattern similar to CFO (see Fig. 10). Next, we calculated the tilting and rotation angles (defined as $\alpha = (180 - \theta)/2$ and $\beta = (90 - \phi)$ respectively where

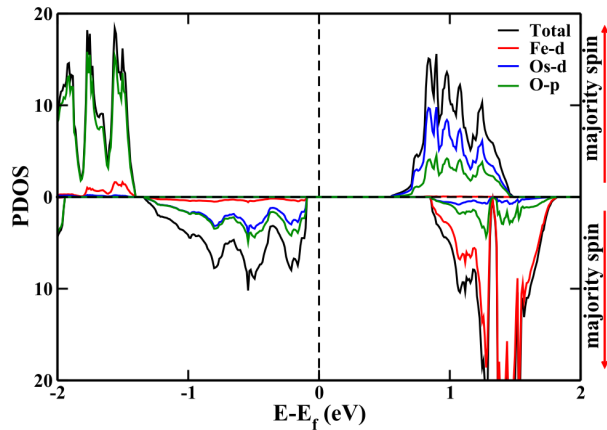
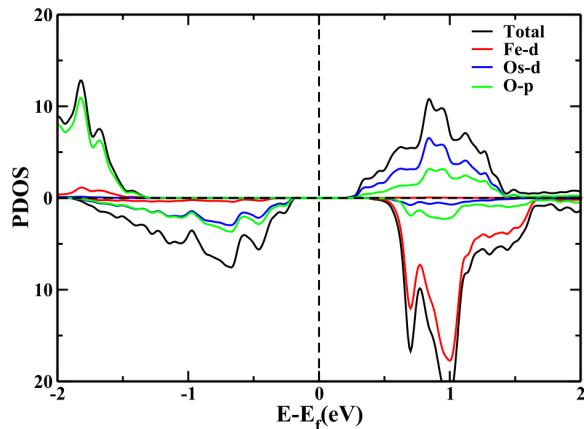
(a) $\lambda = +1$ (b) $\lambda = 0$

FIG. 7. Total and projected density of states (DOS) of the (a) $\lambda = +1$ and (b) $\lambda = 0$ nonpolar structure of CaZnFeOsO_6 . The black, red, blue, and green lines represent the total DOS, and projected DOS of Fe-3d, Os-5d, and O-2p states, respectively. The dotted, vertical line in the plot marks the position of the Fermi level.

angle θ and ϕ are as shown in Figure 11 and compared with the parent CFO. There are two types of rotation angles, denoted as β_1 and β_2 . Since there are two layers within one unit cell containing a total of 20 atoms, each layer is defined by specific rotation angles. These angles are represented as β_{11} and β_{12} for the first layer, and β_{21} and β_{22} for the second layer, as shown in Table I. The subscripts 11/12 correspond to ϕ_1 for the first layer, while 21/22 corresponds to ϕ_2 for the second layer of the transition metal (TM). Regarding the tilting angles, there are also two types, but they have the same value. Therefore, the average value of the tilting angle, denoted

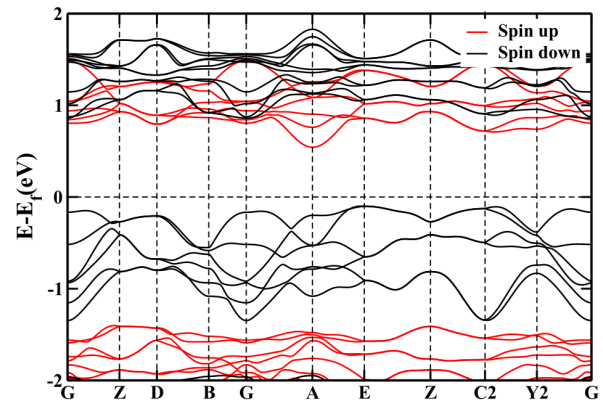


FIG. 8. Calculated band dispersion for the polar $\lambda = +1$ of CaZnFeOsO_6 . The dashed horizontal black line at zero energy marks the position of Fermi energy (E_f). The red line stands for spin-up channel bands, and the black line represents spin-down states. The dotted, black vertical line in the plot marks the position of high-symmetric k points of the Brillouin zone.

as α , was considered. Table I illustrates that the tilting angle increases as the smaller-sized Zn cation is doped at the A-site, resulting in more tilted octahedra. This increase in the tilting angle is attributed to the movement of oxygen anions towards the smaller Zn cations, forming stronger covalent-type bonds. This phenomenon can potentially contribute to the polarization observed in CZFOO. Additionally, the rotation angles also exhibit a slight increase compared to $\text{Ca}_2\text{FeOsO}_6$. In summary, the changes in the tilting and rotation of oxygen octahedra facilitate the development of polarization in CZFOO. Furthermore, we have conducted calculations to deter-

TABLE I. Rotation and tilt angle of oxygen octahedra

Angle	$\text{Ca}_2\text{FeOsO}_6$	CaZnFeOsO_6
α	15.83	19.42
Layer1 β_{11}	10.55	12.02
β_{12}	-10.55	-11.99
Layer2 β_{21}	10.70	11.91
β_{22}	-10.70	-11.91

mine the octahedral distortion parameter (Δ_d) for both $\text{Ca}_2\text{FeOsO}_6$ and CZFOO, as described in ref [34]. The Δ_d parameter quantifies the deviation of the M-O distances from the average $\langle M-O \rangle$ value, providing insight into the overall octahedral distortion in the materials. It can be calculated using root mean square deviation from

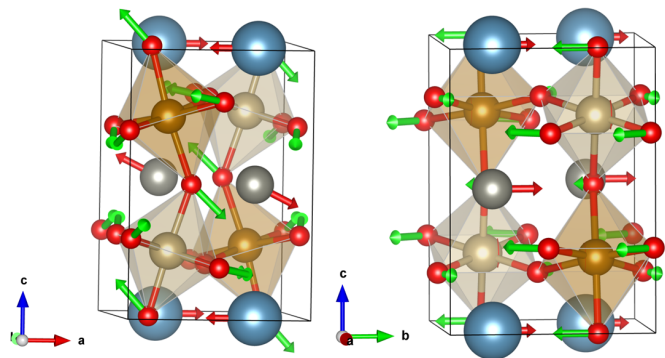
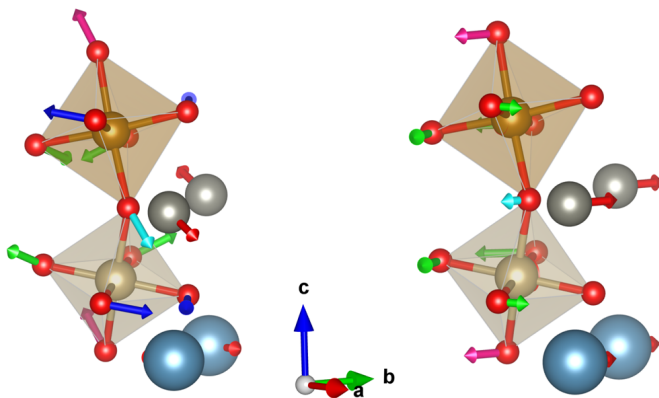
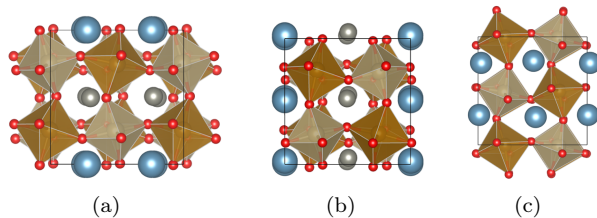
(a) Γ_1^+ and Γ_1^- for 20 atom cell(b) Octahedra rotation and atomic displacement in Γ_1^+ and Γ_1^-

FIG. 9. Two major crystallographic symmetry modes relating the high symmetry nonpolar $P2_1/m$ phase and polar $P2_1$ phase (a) Γ_1^+ and Γ_1^- for 20 atom cell (b) Octahedra rotation and atomic displacement in Γ_1^+ and Γ_1^- mode shown by arrows. Blue and green colors indicate up and down type rotation in Γ_1^+ respectively, whereas green arrows indicate in-plane rotation in Γ_1^- mode. Red arrow indicating the atomic displacement in both modes

FIG. 10. Glazer notation $a^- a^- c^+$ (a) along the a-axis, (b) along the b-axis and (c) along c-axis for $\lambda = +1$ structure

the average formula :

$$\Delta_d = \sqrt{\frac{1}{6} \sum_{n=1,6} [d_i - d_{avg}]^2}$$

Here, d_i represents the individual M-O distances, and d_{avg} denotes the average M-O distance. The obtained

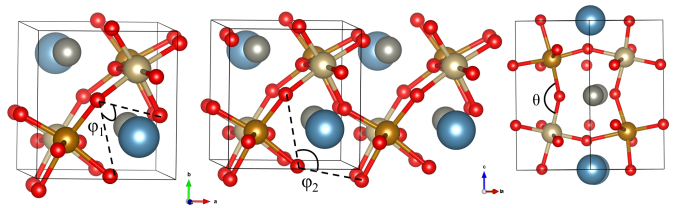


FIG. 11. CZFOO with (rotation) tilting of the octahedral cages. The angles shown define degrees of rotation and tilting.

results, presented in Table II, indicate that CZFOO exhibits a more significant overall octahedral distortion compared to Ca_2FeOsO_6 . This outcome is attributed to the presence of two different-sized A-site cations in CZFOO, which introduces an additional factor contributing to the distortion of the octahedral structure.

TABLE II. Octahedra distortion Δ_d in (\AA) for Ca_2FeOsO_6 and polar CZFOO structure

Δ_d (\AA)	CZFOO ($\lambda = +1$)	Ca_2FeOsO_6	CZFOO ($\lambda = -1$)
Fe1-O	0.0797	0.0052	0.0798
Fe2-O	0.0797	0.0052	0.0798
Os1-O	0.0378	0.0124	0.0379
Os2-O	0.0378	0.0124	0.0379

To further validate the origin of polarization in CZFOO, a symmetry mode analysis was performed using the AMPLIMODES software [33]. This analysis provides a structural decomposition based on symmetry modes. The results revealed the presence of two symmetry-lowering modes with irreducible representations Γ_1^+ and Γ_1^- , as depicted in Figure 9(a). The Γ_1^- mode corresponds to a polar mode with $P2_1$ symmetry. It involves in-plane rotation of the octahedra and the parallel displacement of A-site cations along the b-direction, as shown in Figure 9(b). This mode contributes significantly to the polarization in CZFOO. On the other hand, the Γ_1^+ mode is a non-polar mode with $P2_1/m$ symmetry. In this mode, the A-site atoms undergo displacements in opposite directions, while the oxygen atoms move in a way that preserves the symmetry, as shown in Figure 9(b). The overall rotation of the octahedra does not contribute significantly to the polarization. The global distortion amplitude analysis provides further insights. The distortion amplitude for the Γ_1^- mode is 100%, indicating its dominant role in the transformation from the non-polar $P2_1/m$ phase to the polar $P2_1$ phase (Figure 9(b)). In contrast, the distortion amplitude for the Γ_1^+ mode is 0.00%, confirming its non-polar nature (see Table S2). So, the symmetry mode analysis demonstrates that the Γ_1^- mode is the primary mode responsible for the trans-

formation from the non-polar $P2_1/m$ phase to the polar $P2_1$ phase in CZFOO. This mode involves in-plane octahedral rotation and the parallel displacement of A-site cations, contributing significantly to the observed polarization.

TABLE III. Magnetic anisotropic energy and magnetization including SOC in $\lambda = +1$

Magnetic moment along	$\Delta E(\text{meV})$	Magnetic moment μ_B/cell		
		mx	my	mz
X-axis	0.00	-0.55	-0.00	4.36
Y-axis	4.21	-0.00	0.00	4.32
Z-axis	9.64	-0.48	-0.00	4.30

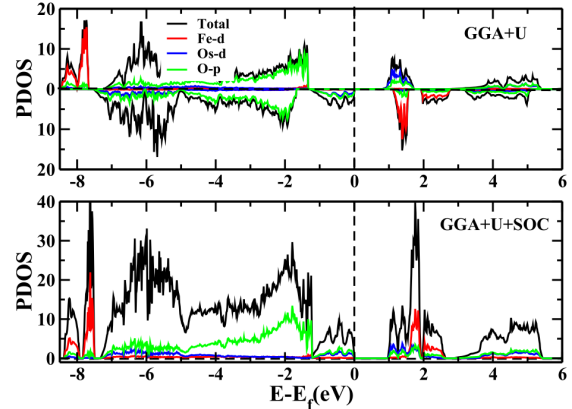
TABLE IV. Magnetic anisotropic energy and magnetization including SOC in $\lambda = -1$

Magnetization axis along	$\Delta E(\text{meV})$	Magnetic moment μ_B/cell		
		mx	my	mz
X-axis	0.00	-0.56	-0.00	4.36
Y-axis	4.14	0.00	0.00	4.32
Z-axis	9.64	-0.41	-0.00	4.30

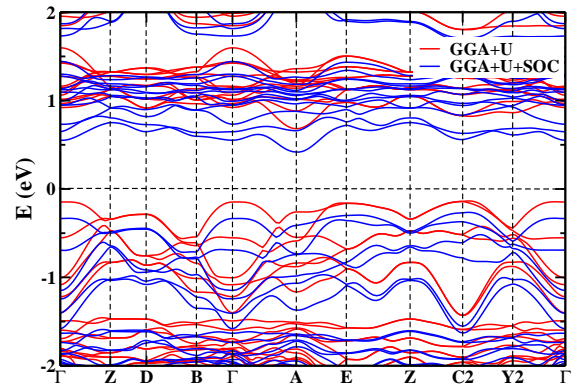
Magnetic anisotropy and Magnetoelectric effect:

Magnetic anisotropy is a critical property in permanent magnets, as it determines their ability to maintain a stable magnetization direction. Materials with high magnetocrystalline energy exhibit desirable qualities for various applications, including magnetic storage devices [35, 36]. The presence of spin-orbit coupling (SOC) and structural distortion contributes significantly to the generation of non-collinear magnetic states and spin canting, which can induce magnetocrystalline anisotropy (MCA) and the magnetoelectric effect (ME) [6]. To investigate the impact of SOC and assess the potential for ME coupling in the system, we employed the GGA+U+SOC method using the Vienna Ab-initio Simulation Package (VASP). The DOS revealed an energy gap of approximately 1 eV between the valence and conduction bands. Notably, the major contributions near the Fermi level originate from the Os-5d and O-2p orbitals, as depicted in Figure 12(a). These orbitals are responsible for the electronic states relevant to the magnetization and magnetoelectric properties of the material.

By considering the electronic band structure with SOC, we can observe the shifting of bands near the Fermi level and a slight opening of the energy gap compared to the band structure obtained using the GGA+U method



(a) Comparison of DOS with SOC



(b) Band structure for GGA+U and GGA+U+SOC

FIG. 12. Comparative plots for (a) total and projected density of states with GGA+U and GGA+U+SOC (b) band structure with GGA+U (red) and GGA+U+SOC (blue)

without SOC, as shown in Figure 12(b). This demonstrates the influence of SOC on the electronic structure and highlights its potential impact on the magnetic and magnetoelectric properties of the system. These findings provide valuable insights into the potential for magnetocrystalline anisotropy and magnetoelectric effects in the system under investigation. Next, we investigated the magnetic anisotropy in CZFOO by varying the magnetization axis in three directions: x, y, and z. We calculated the corresponding energies and found that CZFOO exhibits magnetic anisotropy. The easy axis of magnetization was determined to be along the x-axis, as it possessed the lowest energy compared to the y and z directions. The energy differences for the easy axis were 4.21 and 9.64 meV/cell for the y and z directions, respec-

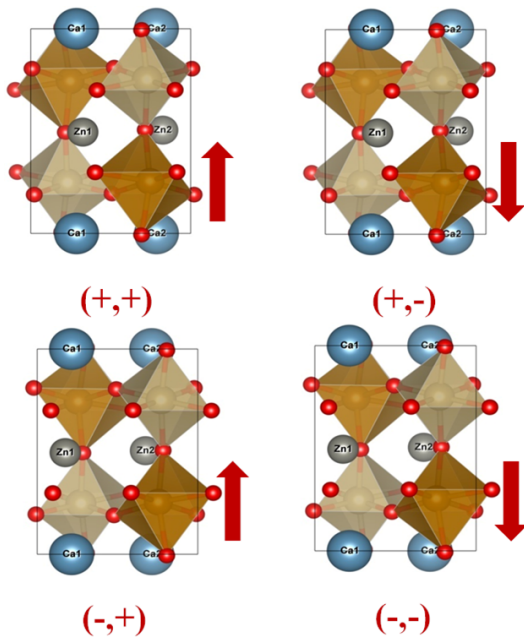


FIG. 13. Four possible configuration for analysing MAE where first sign (+/-) represent the direction of polarization and second sign (+/-) represent the direction of magnetization

tively. Although the magnetic anisotropy energy (MAE) in CZFOO is weaker compared to other multiferroic double perovskites (DPs) [9], it is still larger than the MAE observed in $\text{Ca}_2\text{FeOsO}_6$ (as shown in Table S6). The magnitude of MAE and direction can be further manipulated by considering epitaxial strain. Table III provides

TABLE V. Magnetic moment per atom after applying SOC in polar CZFOO

Magnetic atom	Magnetic moment μ_B/cell		
	mx	my	mz
Fe1	-0.04	0.071	4.224
Os1	-0.165	0.135	-1.901
Os2	-0.164	-0.135	-1.901
Fe2	-0.04	-0.071	4.224

the magnetic moments along the x, y, and z axes for the case of $\lambda = +1$, which exhibits magnetic anisotropy along the x-axis. Similarly, Table IV presents the magnetic moments for the case of $\lambda = -1$, which also shows magnetic anisotropy along the x-axis. Furthermore, Table V displays the non-zero magnetic moments per atom along all three directions with respect to the easy axis (x-axis). It is worth noting that the pictorial representation of the spin alignment, as shown in Figure S4, indicates that the spins are arranged in a collinear manner. This means that there is no significant spin canting even after

applying spin-orbit coupling (SOC).

In our investigation of the coupling between magnetization and electric polarization, we considered four sets of optimized structures denoted as (+,+), (+,-), (-,-), and (-,+) as shown in Figure 13. The first sign represents the polarization direction, while the second sign represents the magnetization direction.

To assess the magnetoelectric coupling in CZFOO, we compared the total energies of these four states, considering the GGA+U+SOC method. The results are summarized in Table VI, where a small energy difference is observed for the structures with inverted spins (180° difference). However, it is important to note that this energy difference is not significant for magnetoelectric coupling, indicating that there is weak coupling present in CZFOO due to the presence of spin-orbit coupling (SOC) [37]. The weak coupling suggests that the flipping of spins by 180° on the application of an electric field is not an easy task, as mentioned in the literature [38]. So, our calculations reveal a weak magnetoelectric coupling in CZFOO due to the small energy differences observed for the four sets of structures with inverted spins. Considering the difficulty in achieving 180° flipping of spins and the need to analyze spin configurations at different angles, further investigation is necessary to fully comprehend the magnetoelectric properties of CZFOO. The magnetoelectric effect in $\text{Zn}_2\text{FeOsO}_6$ stands in contrast to the weak effect observed in CZFOO. The contrasting magnetoelectric effects between CZFOO and $\text{Zn}_2\text{FeOsO}_6$ arise from the different behaviors of their ferroelectric polarizations and the orientations of their easy planes of magnetization.

TABLE VI. Energy difference among different orientation structures

Difference between structures	$\Delta E(\text{meV})$
$E_{(+,+)} - E_{(+,-)}$	0.033
$E_{(-,-)} - E_{(-,+)}$	0.034
$E_{(+,+)} - E_{(-,-)}$	-0.059
$E_{(+,-)} - E_{(-,+)}$	-0.059

CONCLUSIONS:

In summary, we present a novel multiferroic double perovskite compound, CaZnFeOsO_6 , showcasing remarkable ferroelectric and ferrimagnetic properties. Through comprehensive density functional theory calculations, we identify CZFOO as a unique A-site and B-site ordered double perovskite structure, $\text{AA}'\text{BB}'\text{O}_6$. The compound exhibits remarkable ferroelectricity and ferrimagnetism, with substantial magnetization generated by Fe^{3+} and Os^{5+} ions, and a layerwise polar environment created

by Ca^{2+} and Zn^{2+} ions. Specifically, CZFOO showcases a large spontaneous polarization of $16.8 \mu\text{C}/\text{cm}^2$ and a magnetic moment of approximately $2\mu_B$ per formula unit, surpassing those of other double perovskites. However, a weak spin-orbit coupling limits the magnetoelectric effect in CZFOO. Furthermore, our investigation reveals that CZFOO possesses in-plane magnetocrystalline anisotropy along the x-axis. Importantly, by manipulating the epitaxial strain, we can precisely modulate and manipulate the in-plane magnetocrystalline anisotropy, enabling enhanced control over the magnetic behavior and opening up opportunities for novel device applications. Overall, our research highlights the remarkable tunability of the in-plane magnetocrystalline anisotropy in CZFOO through epitaxial strain, providing valuable insights for the design and fabrication of next-generation multiferroic devices with tailored magnetic properties.

* vardha@iiserb.ac.in

- [1] Yoshinori Tokura. *Colossal magnetoresistive oxides*. CRC Press, 2000.
- [2] K-I Kobayashi, T Kimura, Y Tomioka, H Sawada, K Terakura, and Y Tokura. Intergrain tunneling magnetoresistance in polycrystals of the ordered double perovskite $\text{Sr}_2\text{FeReO}_6$. *Physical Review B*, 59(17):11159, 1999.
- [3] K-I Kobayashi, T Kimura, H Sawada, K Terakura, and Y Tokura. Room-temperature magnetoresistance in an oxide material with an ordered double-perovskite structure. *Nature*, 395(6703):677–680, 1998.
- [4] S Mtougui, S Idrissi, H Labrim, N El Mekkaoui, I El Housni, S Ziti, R Khalladi, and L Bahmad. Ground state phase diagrams and magnetic properties of the double perovskite $\text{Pb}_2\text{FeReO}_6$. *arXiv preprint arXiv:2002.08122*, 2020.
- [5] AJC Buurma, GR Blake, TTM Palstra, and Umut Adem. Multiferroic materials: physics and properties. *Reference Module in Materials Science and Materials Engineering*, 2016.
- [6] Shuai Dong, Hongjun Xiang, and Elbio Dagotto. Magnetoelectricity in multiferroics: a theoretical perspective. *National Science Review*, 6(4):629–641, 2019.
- [7] Masaki Azuma, Kazuhide Takata, Takashi Saito, Shintaro Ishiwata, Yuichi Shimakawa, and Mikio Takano. Designed ferromagnetic, ferroelectric $\text{Bi}_2\text{NiMnO}_6$. *Journal of the American Chemical Society*, 127(24):8889–8892, 2005.
- [8] R Nechache, C Harnagea, and A Pignolet. Multiferroic properties—structure relationships in epitaxial $\text{Bi}_2\text{FeCrO}_6$ thin films: recent developments. *Journal of Physics: Condensed Matter*, 24(9):096001, 2012.
- [9] Marjana Ležaić and Nicola A Spaldin. High-temperature multiferroicity and strong magnetocrystalline anisotropy in 3d-5d double perovskites. *Physical Review B*, 83(2):024410, 2011.
- [10] Hong Jian Zhao, Wei Ren, Yurong Yang, Jorge Íñiguez, Xiang Ming Chen, and L Bellaiche. Near room-temperature multiferroic materials with tunable ferromagnetic and electrical properties. *Nature communications*, 5(1):1–7, 2014.
- [11] Joshua Young, Alessandro Stroppa, Silvia Picozzi, and James M Rondinelli. Tuning the ferroelectric polarization in $\text{AA}'\text{MnWO}_6$ double perovskites through a cation substitution. *Dalton Transactions*, 44(23):10644–10653, 2015.
- [12] Hai L Feng, Masao Arai, Yoshitaka Matsushita, Yoshihiro Tsujimoto, Yanfeng Guo, Clastin I Sathish, Xia Wang, Ya-Hua Yuan, Masahiko Tanaka, and Kazunari Yamaura. High-temperature ferrimagnetism driven by lattice distortion in double perovskite $\text{Ca}_2\text{FeOsO}_6$. *Journal of the American Chemical Society*, 136(9):3326–3329, 2014.
- [13] Nicole A Benedek and Craig J Fennie. Why are there so few perovskite ferroelectrics? *The Journal of Physical Chemistry C*, 117(26):13339–13349, 2013.
- [14] PS Wang, W Ren, L Bellaiche, and HJ Xiang. Predicting a ferrimagnetic phase of $\text{Zn}_2\text{FeOsO}_6$ with strong magnetoelectric coupling. *Physical review letters*, 114(14):147204, 2015.
- [15] Man-Rong Li, Peter W Stephens, Maria Retuerto, Tapati Sarkar, Christoph P Grams, Joachim Hemberger, Mark C Croft, David Walker, and Martha Greenblatt. Designing polar and magnetic oxides: $\text{Zn}_2\text{FeOsO}_6$ in search of multiferroics. *Journal of the American Chemical Society*, 136(24):8508–8511, 2014.
- [16] A Savage. Pyroelectricity and spontaneous polarization in linbo_3 . *Journal of Applied Physics*, 37(8):3071–3072, 1966.
- [17] S Mangin, D Ravelosona, JA Katine, MJ Carey, BD Terris, and Eric E Fullerton. Current-induced magnetization reversal in nanopillars with perpendicular anisotropy. *Nature materials*, 5(3):210–215, 2006.
- [18] B Dieny and M Chshiev. Perpendicular magnetic anisotropy at transition metal/oxide interfaces and applications. *Reviews of Modern Physics*, 89(2):025008, 2017.
- [19] S Ikeda, K Miura, H Yamamoto, K Mizunuma, HD Gan, M Endo, SI Kanai, J Hayakawa, F Matsukura, and H Ohno. A perpendicular-anisotropy coFe_2MnGe magnetic tunnel junction. *Nature materials*, 9(9):721–724, 2010.
- [20] Paresch C Rout and Udo Schwingenschlögl. $\text{Ca}_2\text{FeOsO}_6$ superlattice: Multiferroicity above room temperature with giant hybrid-improper ferroelectric polarization and high photovoltaic efficiency. *Physical Review B*, 107(9):094419, 2023.
- [21] Saurabh Ghosh, Hena Das, and Craig J Fennie. Linear magnetoelectricity at room temperature in perovskite superlattices by design. *Physical Review B*, 92(18):184112, 2015.
- [22] Qingyu Lei, Maryam Golalikhani, Bruce A Davidson, Guozhen Liu, Darrell G Schlom, Qiao Qiao, Yimei Zhu, Ravini U Chandrasena, Weibing Yang, Alexander X Gray, et al. Constructing oxide interfaces and heterostructures by atomic layer-by-layer laser molecular beam epitaxy. *npj Quantum Materials*, 2(1):10, 2017.
- [23] John P Perdew, Kieron Burke, and Matthias Ernzerhof. Generalized gradient approximation made simple. *Physical review letters*, 77(18):3865, 1996.
- [24] Matteo Cococcioni and Stefano De Gironcoli. Linear response approach to the calculation of the effective interaction parameters in the LDA+U method. *Physical Review B*, 71(3):035105, 2005.

- [25] Paolo Giannozzi, Stefano Baroni, Nicola Bonini, Matteo Calandra, Roberto Car, Carlo Cavazzoni, Davide Ceresoli, Guido L Chiarotti, Matteo Cococcioni, Ismaila Dabo, et al. Quantum espresso: a modular and open-source software project for quantum simulations of materials. *Journal of physics: Condensed matter*, 21:395502, 2009.
- [26] RD King-Smith and David Vanderbilt. Theory of polarization of crystalline solids. *Physical Review B*, 47(3):1651, 1993.
- [27] Georg Kresse and Jürgen Furthmüller. Efficiency of ab-initio total energy calculations for metals and semiconductors using a plane-wave basis set. *Computational materials science*, 6(1):15–50, 1996.
- [28] Almudena Notario-Estévez Sergey M Kozlov, Francesc Viñes, and Francesc Illas. Electronic-structure-based chemical descriptors:(in) dependence on self-interaction and hartree-fock exchange. *Phys. Rev. B*, 54:11169–11186, 1996.
- [29] Georg Kresse and Daniel Joubert. From ultrasoft pseudopotentials to the projector augmented-wave method. *Physical review b*, 59(3):1758, 1999.
- [30] Stefano Baroni, Stefano De Gironcoli, Andrea Dal Corso, and Paolo Giannozzi. Phonons and related crystal properties from density-functional perturbation theory. *Reviews of modern Physics*, 73(2):515, 2001.
- [31] G Kresse, J Furthmüller, and J Hafner. Ab initio force constant approach to phonon dispersion relations of diamond and graphite. *EPL (Europhysics Letters)*, 32(9):729, 1995.
- [32] K Parlinski, ZQ Li, and Y Kawazoe. First-principles determination of the soft mode in cubic ZrO₂. *Physical Review Letters*, 78(21):4063, 1997.
- [33] Mois I Aroyo, Asen Kirov, Cesar Capillas, JM Perez-Mato, and Hans Wondratschek. Bilbao crystallographic server. ii. representations of crystallographic point groups and space groups. *Acta Crystallographica Section A: Foundations of Crystallography*, 62(2):115–128, 2006.
- [34] JA Alonso, MJ Martinez-Lope, MT Casais, and MT Fernandez-Diaz. Evolution of the jahn-teller distortion of mno₆ octahedra in RMnO₃ perovskites (R= Pr, Nd, Dy, Tb, Ho, Er, Y): a neutron diffraction study. *Inorganic chemistry*, 39(5):917–923, 2000.
- [35] John MD Coey. *Magnetism and magnetic materials*. Cambridge university press, 2010.
- [36] JMD Coey. Hard magnetic materials: A perspective. *IEEE Transactions on magnetics*, 47(12):4671–4681, 2011.
- [37] Silvia Picozzi, Kunihiro Yamauchi, Biplab Sanyal, Ivan A Sergienko, and Elbio Dagotto. Dual nature of improper ferroelectricity in a magnetoelectric multiferroic. *Physical Review Letters*, 99(22):227201, 2007.
- [38] Claude Ederer and Nicola A Spaldin. Weak ferromagnetism and magnetoelectric coupling in bismuth ferrite. *Physical Review B*, 71(6):060401, 2005.